Evaluating the effectiveness of CFD-DEM and SPH-DEM for complex pipe flow simulations with and without particles

Yang, Zhuangjian; Lian, Xue; Savari, Chiya; Barigou, Mostafa

DOI:
10.1016/j.ces.2024.119788

Document Version
Publisher's PDF, also known as Version of record

Citation for published version (Harvard):
Yang, Z, Lian, X, Savari, C & Barigou, M 2024, 'Evaluating the effectiveness of CFD-DEM and SPH-DEM for complex pipe flow simulations with and without particles', *Chemical Engineering Science*, vol. 288, 119788. https://doi.org/10.1016/j.ces.2024.119788

Chemical Engineering Science 288 (2024) 119788

Contents lists available at ScienceDirect

Chemical Engineering Science

journal homepage: www.elsevier.com/locate/ces

Evaluating the effectiveness of CFD-DEM and SPH-DEM for complex pipe flow simulations with and without particles

ZhuangJian Yang [1], Xue Lian [1], Chiya Savari, Mostafa Barigou [*]

School of Chemical Engineering, University of Birmingham, Edgbaston, Birmingham B15 2TT, UK

ARTICLE INFO

Keywords:
CFD
DEM
SPH
Pipe flow
Particle-liquid flow
PEPT

ABSTRACT

We investigate the effectiveness of two computational fluid dynamics (CFD) approaches: mesh-based CFD and meshfree particle-based smoothed particle hydrodynamics (SPH) for simulating pipe flows of varying complexity. The study covers laminar and turbulent flows, different fluid rheologies (Newtonian, power-law, Bingham plastic, Herschel-Bulkley), and different particle-laden scenarios, validated using experimental Lagrangian measurements obtained by positron emission particle tracking or available theoretical solutions, as appropriate. We assess these methods based on their ability to predict radial profiles of local phase velocity and concentration, as well as computational cost. In single-phase flows, CFD aligns well with experimental data and theoretical models. SPH exhibits boundary discrepancies due to no-slip condition approximations and limitations in turbulent flow simulation which need further development. Integrating the discrete element method (DEM) significantly enhances both techniques for particle-liquid flows. Mesh-based CFD is computationally efficient, while particle-based SPH can offer more insights into Lagrangian fluid dynamics.

1. Introduction

Single-phase and particle-liquid pipe flows play a crucial role in various industries, such as mining, pharmaceuticals, food processing, chemicals, oil and wastewater treatment. These flows are characterized by a number of complexities, including intiricate pipe geometries, diverse liquid rheologies, different flow regimes and phase-to-phase interactions, which present significant challenges for design, operation and control. The advancement in computational capabilities over the past decades has led to the emergence of powerful computational fluid dynamics (CFD) tools, encompassing both mesh and meshfree methods. These tools have great potential for simulating and predicting complex flows of complex fluids, offering a viable route for numerical investigation and optimization of multiphase flows for various engineering applications (El-Emam et al., 2021; Ye et al., 2019).

The mesh-based CFD approach is mature and widely used. It includes techniques such as the finite element method (FEM), the finite volume method (FVM) and the finite difference method (FDM) which have been exploited in different applications under a variety of geometries, scales and conditions, such as fluidized beds (Zbib et al., 2018), stirred vessels (Liu and Barigou, 2013), particle combustion (Kong et al., 2021), viscous pipe flow (Eesa and Barigou, 2008), and blood flow (Bose and Banerjee, 2015). The primary fluid phase is normally simulated by solving the Navier–Stokes equations in each cell inside the mesh using an Eulerian approach (Liu et al., 2017; Sharaf et al., 2019). When a secondary discrete phase, such as a particulate phase, is introduced into the primary Euerlian phase, two different approaches may be used: the Eulerian-Lagrangian (EL) approach considers the particulate phase as a discrete phase and estimates particle motions individually (Tian and Barigou, 2016), whereas the Eulerian-Eulerian (EE) approach which is computationally less expensive treats the particulate phase as a continuum (Messa and Matoušek, 2020). Each approach offers distinct advantages and is selected based on the specific characteristics and requirements of the multiphase flow being analyzed.

The mesh method suffers from limitations in handling certain complex problems involving large mesh deformations, deformable and growing boundaries and free surface phenomena (Belytschko et al., 1996). Thus, the alternative meshfree method has attracted increasing attention over the past decades due to its ability to address these challenging situations (Ye et al., 2019). Specifically, for modeling intricate fluid flows, researchers have explored meshfree particle-based methods, such as the moving particle semi-implicit (MPS) and smoothed particle hydrodynamics (SPH) techniques (Duan et al., 2017; Liu and Liu, 2010).

* Corresponding author.
E-mail address: m.barigou@bham.ac.uk (M. Barigou).
[1] These two authors contributed equally.

https://doi.org/10.1016/j.ces.2024.119788
Received 3 October 2023; Received in revised form 1 December 2023; Accepted 17 January 2024
Available online 20 January 2024

Nomenclature

Symbols

C_s	volumetric mean solid concentration, vol.%
c	local volumetric solid concentration. vol.%
D	pipe diameter, m
d_p	particle diameter, m
h	Kernel smooth length, m
m	Papanastasiou parameter
n	power-law index
r	radial position, m
R	pipe radius, m
Re	pipe Reynolds number
Re_p	particle Reynolds number
Re_{mean}	Particle-liquid flow mixture Reynolds number
t	time, s
u_L	axial liquid velocity, m s^{-1}
u_S	axial particle velocity, m s^{-1}
u_{mean}	mean mixture velocity, m s^{-1}

Greek Symbols

υ	kinematic viscosity, m^2 s^{-1}
μ_L	viscosity, kg m^{-1} s^{-1}
ρ_L	liquid density, kg m^{-3}
ρ_s	particle density, kg m^{-3}
ρ_r	particle to liquid density ratio

Abbreviations

CFD	Computational Fluid Dynamics
CMC	Carboxymethyl Cellulose
DEM	Discrete Element Method
EE	Eulerian-Eulerian
EL	Eulerian-Lagrangian
FEM	Finite Element Method
FVM	Finite Volume Method
LDV	Laser Doppler Velocimetery
MPS	Moving Particle Semi-implicit
PEPT	Positron Emission Particle Tracking
PIV	Particle Image Velocimetery
SPH	Smoothed Particle Hydrodynamics

MPS transforms the governing equations into interactions among moving particles and employs a semi-implicit algorithm to handle incompressible flows (Koshizuka and Oka, 1996). On the other hand, SPH initially developed for astrophysics nearly 40 years ago (Lucy (1977), has been extended to tackle a variety of fluid and solid mechanics problems. It approximates field variables (e.g., density, velocity, acceleration) on a set of particles and does not rely on a fixed mesh, making it well-suited for capturing complex fluid information and accommodating large deformations (Lucy, 1977). Moreover, it naturally tracks free surfaces, moving boundaries and interfaces, enabling its application to multiphase flows by representing these features as particles defined at the initial stage, thus, overcoming the challenges faced by conventional mesh-based CFD methods. Additionally, SPH exhibits excellent conservation properties and satisfactorily handles interface tracking in multiphase flows. Combining meshfree, particle-based and Lagrangian characteristics, SPH offers distinct advantages over CFD methods (Ye et al., 2019), making it a promising and valuable tool for computational fluid dynamics simulations.

The discrete element method (DEM) is a numerical simulation technique used in engineering and physics to model the behaviour of essentially dry granular materials and other discrete systems. It treats individual particles as distinct entities, each possessing specific properties such as mass, shape and interactions with other particles. By simulating the motion and interactions of such discrete particles over time, DEM can provide insights into complex phenomena like particle flow, collision dynamics and stress distribution in granular materials. Newton's second law is used to track and describe the motion of every single particle (Cundall and Strack, 1979; Nguyen et al., 2022). In recent years, the coupling of DEM with CFD and SPH has emerged as a powerful hybrid approach to study complex multiphase flows and interactions between solid particles and fluids (Lian et al., 2023; Zheng et al., 2021). This coupling involves integrating the granular dynamics of DEM with the fluid flow characteristics modelled by CFD or SPH.

In this paper, we investigate the capability and performance of the mesh-based CFD method and the meshfree particle-based SPH method for simulating the turbulent pipe flow of single-phase Newtonian fluids, as well as the viscous pipe flow of fluids of varying rheologies, namely Newtonian, power-law, Bingham plastic and Herschel-Bulkley. The two numerical techniques are then coupled with DEM to study the viscous and turbulent pipe flows of particle-liquid mixtures under various conditions of particle loading. Experimental measurements obtained by the Lagrangian technique of positron emission particle tracking (PEPT) is used alongside available theoretical solutions, to validate the simulations results, as appropriate. The assessment of the two numerical techniques considers the detailed predictions of radial velocity profiles, spatial particle distributions as well as computational cost. This study serves to advance our understanding of these numerical methods and their capability to simulate complex multiphase flows, providing valuable guidance for future research and practical applications.

2. Experiment and data analysis

2.1. Pipe flow loop set-up

The experimental flow loop used to conduct single-phase flow as well as particle-liquid flow experiments is schematically represented in Fig. 1. In particle-liquid flows, the particle-liquid mixture was continuously held in suspension in a conical tank by a mechanical agitator and circulated through a 4 m long horizontal Perspex pipe of 0.04 m internal diameter by a vortex pump (T21-32 HF4 LB1, Turo vortex pump, EGGER, Switzerland) which guaranteed no particle breakage. Flow visualisation was conducted along a 0.4 m section, located 3 m downstream of the pipe inlet where flow was fully developed. The volumetric flowrate was determined using two independent techniques: direct reading from a Doppler flow meter (UFD5500, Doppler flow meter, Micronics) and by using a stopwatch and bucket. The liquids used were an aqueous 0.8 wt% carboxymethyl cellulose (CMC) solution for laminar flows and an aqueous 36 wt% sugar solution for turbulent cases. The solid phase consisted of 4 mm nearly-neutrally buoyant calcium alginate particles, fabricated using the protocol reported in our previous work (Fairhurst et al. (2001). The rheological characteristics of the liquids were measured using a hybrid rheometer (Discovery HR-2, TA, USA) capable of accurate measurements under strain or stress controlled modes. The liquid and solid densities were measured by a density meter (XPR/XSR density kit, Mettler-Toledo Ltd., UK). The temperature, flowrate and other physical properties of particles and liquids were monitored during experiments, helping to produce consistent and reliable results. The properties of the particles and liquids used are summarized in Table 1.

2.2. Positron emission particle tracking

The PEPT technique provides accurate three-dimensional (3D) spatial coordinates over time for a Lagrangian radioactive particle tracer

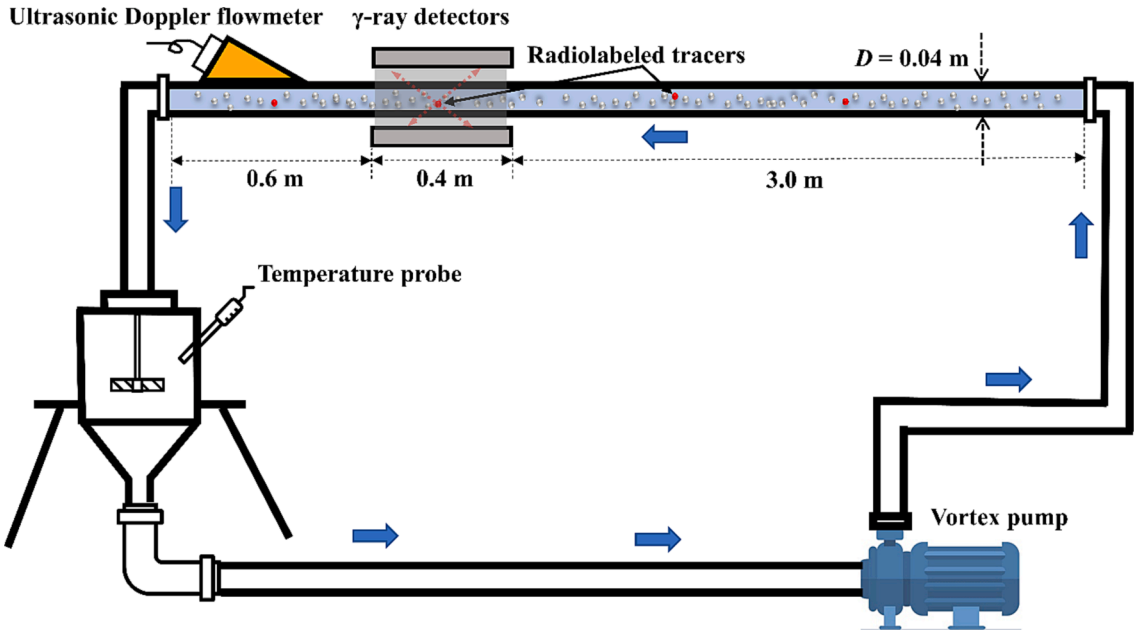

Fig. 1. Schematic of experimental pipe flow loop.

Table 1
Experimental and simulation conditions of single-phase and particle-liquid flows.

Single phase flow						**Particle-liquid flow**		
	Laminar regime				**Turbulent regime**		**Laminar regime**	**Turbulent regime**
	Newtonian	Power-law	Bingham	Herschel–Bulkley	Newtonian			
k_f (Pa s^n)	-	0.02	0.2	0.2	-	d_p (mm)	4.0	4.0
τ_y (Pa)	-	0	1-7	3	-	ρ_s (kg m^{-3})	1014	1165
n (-)	-	0.6-1.4	1	0.6-1.4	-	ρ_L (kg m^{-3})	1000	1143
u_{mean} (m s^{-1})	0.0005-0.025	0.13-0.14	0.036-0.21	0.061-1.35	0.42-2.9	ρ_r (-)	1.014	1.02
$Re_{mean} = \frac{\rho_L D u_{mean}}{\bar{\mu}}$	20-1000	100	100	100	4500-108000	C_s (vol.%)	10, 30	30
						μ_L (Pa s)	-	0.0043
						u_{mean} (m s^{-1})	0.056, 0.083	0.74
						$Re_{mean} = \frac{\rho_L D u_{mean}}{\mu}$	14	7800

suitable for the phase being tracked. The tracer is permitted to circulate around the flow loop until the entire cross-section of the pipe is mapped. A microscopic radiolabelled neutrally-buoyant resin particle was used to track the continuous phase, while a representative alginate particle incorporating at its centre one such radiolabelled resin particle was utilised for the solid phase. In practice, eight such tracers were introduced in the flow to track each phase, reducing experimental time. Being based on γ-ray transmission, PEPT can diagnose complex opaque flows with high particle loadings and inside opaque conduits. The accuracy of PEPT is comparable to that of PIV and LDV. We previously showed that the RMS value of the point differences between two velocity profile curves estimated by PIV and PEPT in a turbulent stirred vessel was within the range 0.02–0.08, which shows a close agreement between the two techniques (Pianko-Oprych et al. (2009). PEPT is a powerful tool for studying the dynamics of particulate systems, such as agitated mixing tanks (Guida et al., 2010; Li et al., 2023a; Liu and Barigou, 2013; Savari et al., 2021) and pipe flows (Fairhurst et al., 2001; Lian et al., 2023). Further detailed information of this well-established technique can be found in our earlier papers (Barigou, 2004; Fairhurst et al., 2001; Guida et al., 2011; Savari and Barigou, 2022; Sheikh et al., 2022b).

2.3. PEPT data processing

To obtain local phase velocities and concentrations from PEPT measurements, two different analysis methods were applied. A regression analysis was applied to obtain the local Lagrangian velocities to enable the construction of the radial velocity distributions of the liquid and particles (Bakalis et al., 2003). For this purpose, the cross-section of the pipe was divided into 40 semi-annular sections of equal area, with 20 above and 20 below the centreline, as depicted in Fig. 2a. The radial mean velocity with its corresponding standard deviation, was calculated from local PEPT velocity values in every semi-annular section.

A 3D grid comprising cells of equal volume was adopted to represent the spatial domain within the pipe (Fig. 2b). Conventionally, the presence of a tracer within each cell has been quantified as the proportion of the total duration of experimental observation (t_∞) during which the tracer occupies that specific cell. However, this quantification is inherently influenced by the density of the grid, thus, the occupancy decreases as the number of cells increases (Guida et al., 2010). To mitigate this inherent bias, the concept of ergodic time (t_E) was introduced as the time a tracer would hypothetically spend within a given cell, assuming that the system behaves as a single-phase and adheres to ergodic principles. For cells of uniform volume, t_E is defined as the total experimental observation time divided by the total count of cells, i.e., $t_E = t_\infty / N_c$. The notion of ergodic time postulates that the tracer possesses an equiprobable likelihood of being located at any point within the pipe volume. As a logical extension, the local occupancy is defined as the temporal interval (Δt) during which the tracer visits a specific cell,

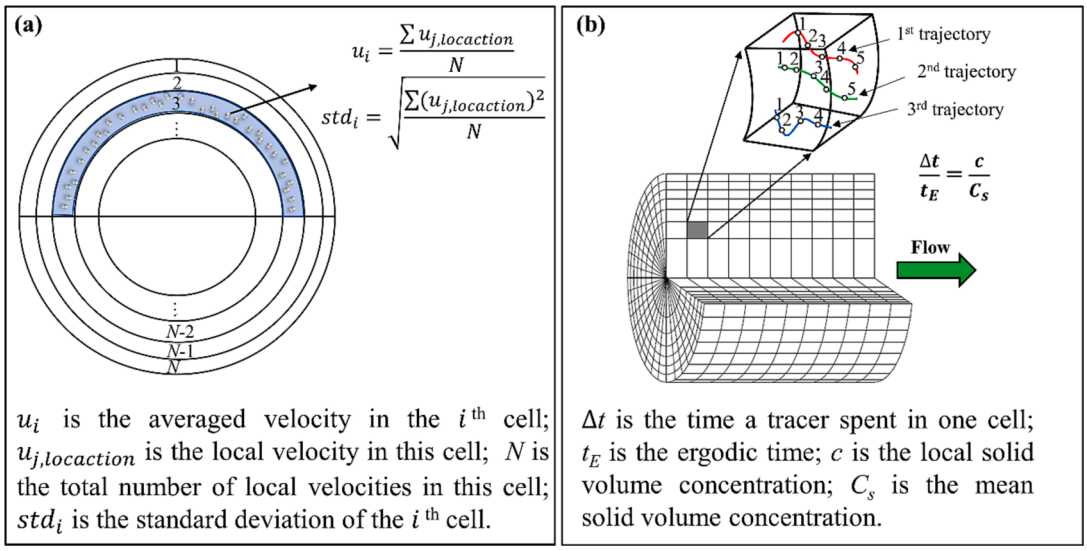

Fig. 2. PEPT data processing of (a) local phase velocities and (b) solid phase distribution.

divided by the ergodic time (t_E). Such a definition, leads to the local occupancy being equivalent to the ratio of the local concentration of solid particles (c) to the mean concentration of solid particles within the pipe (C_s) (Guida et al., 2010; Yang et al., 2022). Further details of PEPT data processing can be found in our previous papers (Li et al., 2022; Li et al., 2023b; Savari et al., 2022; Sheikh et al., 2022a).

3. Numerical methodology

The following sections outline the theory underpinning the mesh-based CFD method and the meshfree particle-based SPH method, as well as their coupling algorithms with the DEM technique.

3.1. Mesh-based CFD method

Simulation of multiphase flow by CFD used the Eulerian-Lagrangian approach by solving the fluid phase as a continuum (Eulerian) and the dispersed phase as a discrete phase within a Langrangian framework by resolving the force balance on each numerical particle.

3.1.1. Continuous phase modelling in CFD

The mass and momentum conservation equations are expressed, respectively, as (Yeoh and Tu, 2019):

$$\frac{\partial}{\partial t}(\alpha_L \rho_L) + \nabla \bullet (\alpha_L \rho_L \vec{u}_L) = 0 \tag{1}$$

and

$$\frac{\partial}{\partial t}\left(\alpha_L \rho_L \vec{u}_L\right) + \nabla \bullet \left(\alpha_L \rho_L \vec{u}_L \vec{u}_L\right) = -\alpha_L \nabla p + \nabla \bullet \left[\alpha_L \mu_L \left(\nabla \vec{u}_L + \nabla \vec{u}_L{}^T\right)\right] + \alpha_L \rho_L \vec{g} + \vec{F} \tag{2}$$

where, α_L, ρ_L, $\vec{u}_L$ and μ_L are the volume fraction, density, velocity and viscosity of the liquid phase. p is the pressure of the whole flow system and g is the gravitational acceleration. $\vec{F}$ represents the forces due to interaction with the discrete phase and is discussed in more detail in section 3.1.4, Eq. (7). When simulating single-phase liquid flow, $\alpha_L = 1$ and $\vec{F} = 0$.

3.1.2. Fluid rheology in viscous flow

To simulate fluids of Newtonian rheology in viscous flow by CFD, the Newtonian model ($\tau = \eta\dot{\gamma}$) with a constant viscosity (η) was used. For more complex rheologies, the power-law and Herschel-Bulkley (HB) models were used to estimate the apparent viscosity (μ) of the liquid phase, respectively, as follows:

$$\mu = k_f \dot{\gamma}^{n-1} \tag{3}$$

and

$$\mu = \begin{cases} \mu = k_f \dot{\gamma}^{n-1} + \frac{\tau_y}{\dot{\gamma}} \tau > \tau_y \\ \mu \to \infty \tau \le \tau_y \end{cases} \tag{4}$$

where, k_f is the fluid consistency index, $\dot{\gamma}$ is the shear rate and n is the flow behaviour index. τ and τ_y are the shear stress and apparent yield stress, respectively. Bingham plastic fluids $\left(\tau = \tau_y + k_f \dot{\gamma}^n\right)$ were simulated using the HB model with $n = 1$.

3.1.3. Turbulence modelling

A number of turbulence models exist. Here, the Reynolds averaged Navier Stoke's (RANS) k-ε model was used:

$$\frac{\partial}{\partial t}(\alpha_L \rho_L k_L) + \nabla \bullet \left(\alpha_L \rho_L \vec{u}_L k_L\right) = \nabla \bullet \left(\alpha_L \left(\mu_L + \frac{u_{t,L}}{\sigma_k}\right) \nabla k_L\right) + \alpha_L G_{k,L} - \alpha_L Y_{k,L} + \alpha_L G_{kb,L} \tag{5}$$

and

$$\frac{\partial}{\partial t}(\alpha_L \rho_L \varepsilon_L) + \nabla \bullet \left(\alpha_L \rho_L \vec{u}_L \varepsilon_L\right) = \nabla \bullet \left(\alpha_L \left(\mu_L + \frac{u_{t,L}}{\sigma_\varepsilon}\right) \nabla \varepsilon_L\right) + \alpha_L G_{\varepsilon,L} - \alpha_L Y_{\varepsilon,L} + \alpha_L G_{\varepsilon b,L} \tag{6}$$

where, k and ε are the turbulent kinetic energy and its dissipation rate; $G_{k,L}$ and $G_{\varepsilon,L}$ are the generation of turbulence kinetic energy and specific dissipation rate; $Y_{k,L}$ and $Y_{\varepsilon,L}$ are the dissipation of turbulence kinetic energy and specific dissipation rate; and $G_{kb,q}$ and $G_{\varepsilon b,q}$ are the generation of turbulence kinetic energy and specific dissipation rate due to buoyancy effects. For flows of low turbulence ($Re < 10{,}000$), the shear stress transportation (SST) model was used (Menter et al., 2003).

3.1.4. Discrete phase modelling in CFD-DEM framework

The Lagrangian model of the mesh-based CFD method was coupled with the DEM method to numerically solve the discrete particle phase. To model the discrete particulate phase behaviour in such CFD-DEM framework, the force balance on each particle is written as:

$$m_p\frac{d\vec{u}_p}{dt} = -\vec{F} = \vec{F}_d + \vec{F}_p + \vec{F}_{lift} + \vec{F}_g + \vec{F}_b + \vec{F}_{vm} + \vec{F}_{td} + \sum_q \vec{F}_{DEM,pq} \tag{7}$$

The total force acting on the particle consists of the drag force ($\vec{F}_d$) which includes a drag force caused by the slip velocity and a drag force due to particle rotation (Dennis et al., 1980), pressure gradient force ($\vec{F}_p$) (Fluent, 2011), Magnus lift force ($\vec{F}_{lift}$) (Tsuji et al., 1985), gravity force ($\vec{F}_g$), buoyancy force ($\vec{F}_b$), virtual mass force ($\vec{F}_{vm}$) (Drew, 1993) and turbulence dispersion force ($\vec{F}_{td}$). To estimate the particle dispersion ($\vec{F}_{td}$) due to turbulence fluctuations, the discrete random walk (DRW) model was applied (Gosman and Loannides, 1983). This model estimates particle movement by characterising a proper interval time (t_{int}) which is the minimum of the eddy lifetime (τ_e) and the time required for a particle to cross this eddy (t_{cross}), expressed as:

$$t_{int} = \min[\tau_e, t_{cross}] \tag{8}$$

where,

$$\tau_e = 2T_L,\quad T_L = C_L\frac{1}{\omega_L};\ t_{cross} = -\tau_p ln\left[1-\tau_p\left(\frac{L_e}{|u_L-u_p|}\right)\right];\ \tau_p = \frac{\rho_p d_p^2}{18\mu_L} \tag{9}$$

T_L is the integration time scale, C_L is a constant equal to 0.15, and ω_L is the liquid specific dispersion rate estimated by the shear stress transport model; L_e is the eddy length scale, u_L is the bulk liquid velocity and u_p is the particle velocity; τ_p is the particle relaxation time, ρ_p is the density of particles and d_p is the particle diameter.

The term ($\vec{F}_{DEM,pq}$) in Eq. (7) represents the collision between particle p and particle q or particle–wall collision force as modelled by the DEM module. The Hertz-Mindlin contact model which combines Hertz's theory in the normal direction and the Mindlin's no-slip model in the tangential direction (Hertz, 1882; Mindlin, 1949), was applied to couple DEM with CFD ($\vec{F}_{DEM,pq}$). The total collision force is the sum of the normal force ($F_{c,n}$) and tangential force ($F_{c,t}$) components, given by:

$$\vec{F}_{DEM,pq} = F_{c,n} + F_{c,t} = \sqrt{\bar{R}\delta_n}(k_n U_n - c_n\bar{m}V_n) + \sqrt{\bar{R}\delta_n}(-k_t U_t - c_t\bar{m}V_t) \tag{10}$$

where, $\bar{R}$ is the effective radius, δ_n is the overlap distance and $\bar{m}$ is effective mass. The quantities of the normal and tangential stiffness and damping coefficients (k_n, k_t, c_n, and c_t) are defined based on materials characteristics, the parameters input by the user, such as modulus of elasticity (E), Poisson's ratio (P_o), Coulomb friction coefficient (e_f) and coefficient of restitution (e). In normal contact, the particle deformation is defined as the penetration of the two particles by $U_n = \delta_n n_n$, where n_n denotes the normal-contact unit vector. In the tangential direction, the deformation is defined by following the total tangential displacement of the initial contact points of the two particles over each time step Δt, $U_t = V_t\Delta t$.

3.2. Meshfree particle-based SPH method

3.2.1. Continuous phase modelling in SPH

SPH models the fluid as a set of numerical particles which interact with each other through a smoothing kernel, as illustrated in Fig. 3. The smoothing kernel is a function determining how information from neighbouring particles is used to compute various physical quantities at a specific numerical particle position. The kernel function defines the spatial influence or weighting of neighbouring particles based on a non-dimensional distance $q_d = |r_{ab}/h|$, where r_{ab} and h are, respectively, the distance between two numerical particles a and b, and smoothing length. There is not a unique way to choose a kernel function in SPH simulations, however, a quintic class 2 Wendland function is commonly used in simulations of multiphase flows (Robinson, 2009):

$$W(r_{ab},h) = \alpha_D\begin{cases}\left(1-\frac{q_d}{2}\right)^4(2q_d+1), & 0\leqslant q_d\leqslant 2,\\ 0, & q_d\geqslant 2,\end{cases} \tag{11}$$

where, $\alpha_D = \frac{7}{4}\pi h^2$ in 2D SPH simulations and $\alpha_D = \frac{21}{16}\pi h^3$ in 3D SPH simulations.

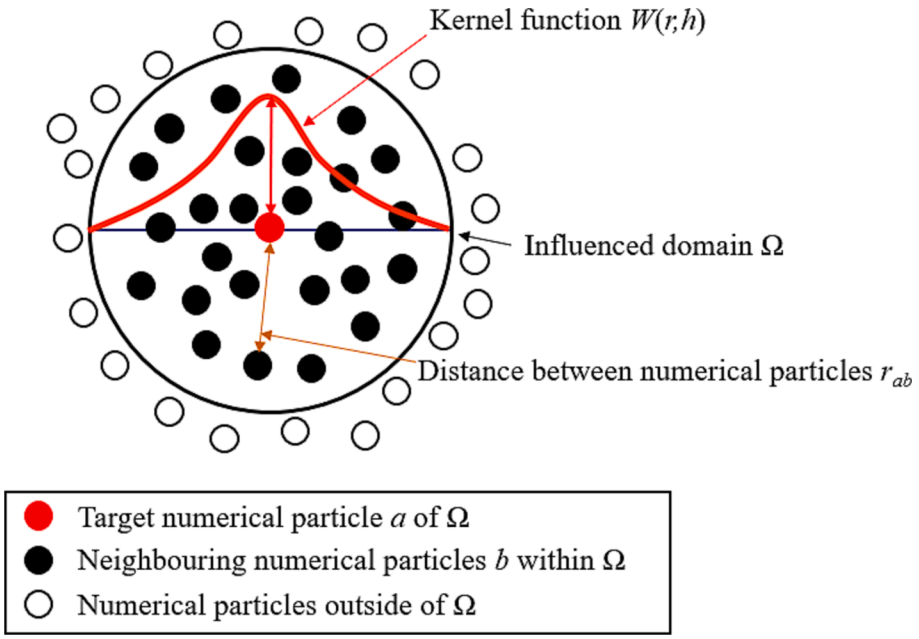

Fig. 3. Schematic of the kernel function in the SPH method.

In SPH, fluid motion is governed by a set of differential equations. The equation of mass conservation computes the density variations in the fluid. To reduce fluid density fluctuations in a 3D simulation, a density diffusion term is introduced into the continuity equation (Fourtakas et al., 2019):

$$\frac{d\rho_a}{dt} = \sum_b m_b v_{ab} \bullet \nabla_a W_{ab} + \delta h c_0 \sum_b 2\left(\rho_{ba}^T - \rho_{ab}^H\right) \frac{r_{ab} \bullet \nabla_a W_{ab}}{r_{ab}^2} \frac{m_b}{\rho_b} \tag{12}$$

where, $v_{ab} = v_a - v_b$ and $r_{ab} = r_a - r_b$ are the velocity difference and separation distance between numerical particles a and b, respectively. The second term on the right-hand side is the density diffusion term, c_0 refers to the speed of sound at the reference density and δ is a coefficient which controls the density diffusion. T and H refer to the total and hydrostatic components of liquid density. The hydrostatic pressure difference between numerical particles a and b is computed as:

$$P_{ab}^H = \rho_0 g z_{ab} \tag{13}$$

where, ρ_0 represents the reference density, usually the density of water, and z_{ab} is the vertical distance between a and b.

In SPH, the relationship between pressure and density is represented by an artificial equation of state (Monaghan, 2005):

$$\mathrm{P} = \mathrm{B}\left[\left(\frac{\rho}{\rho_0}\right)^{\gamma} - 1\right] \tag{14}$$

where, P is pressure, γ is the fluid polytropic index (here, $\gamma = 7$), $B = c_0^2\rho_0/\gamma$, and c_0 refers to the speed of sound at the reference density; c_0 is typically at least 10 times the maximum velocity of the flow. At the end of the simulation, the density variations of numerical particles must be less than 1 % to ensure reliability of results (Gomez-Gesteira et al., 2010).

The Lagrangian form of the momentum conservation equation in SPH is written as:

$$\frac{dv_a}{dt} = -\sum_b m_b \left(\frac{P_a + P_b}{\rho_a \bullet \rho_b}\right) \nabla_a W_{ab} + g + \Gamma_a + S_C \tag{15}$$

where, t is simulation time and v_a is the velocity of numerical particle a; P_a and ρ_a are the pressure and density of numerical particle a; P_b and ρ_b are the pressure and density of numerical particle b. Γ_a is the viscosity terms and g is gravitational acceleration; W_{ab} is the kernel function and S_C is the term of momentum conservation in particle-liquid flow which is expressed as $S_C = f_a/m_a$, where f_a is the whole coupling force acting on the liquid numerical particle a due to neighbouring solid particles.

3.2.2. Fluid rheology in viscous flow

Fluid rheology in viscous flow was modelled in SPH by the Herschel-Bulkley-Papanastasiou (HBP) model (Han et al., 2020). This is a general viscoplastic model which has the advantage of being able to represent various time-independent rheological behaviours including Newtonian, power law, Bingham and Herschel-Bulkley, making it popular for use in numerical simulations. In this model, the effective fluid viscosity (μ_{eff}) is a function of shear rate ($\dot{\gamma}$) and apparent yield stress (τ_y), thus:

$$\mu_{eff} = \mu(\dot{\gamma})^{n-1} + \frac{\tau_y}{2\dot{\gamma}}\left(1 - e^{-m\dot{\gamma}}\right) \tag{16}$$

where, m is the Papanastasiou parameter.

3.2.3. Turbulence modelling

In SPH, the viscosity effects are represented by the viscosity term Γ_a in the momentum equation (Eq. (15)). The laminar viscosity with a sub-particle scale model (SPS) can be expressed as (Dalrymple and Rogers, 2006; Lo and Shao, 2002):

$$\Gamma_a = \sum_b m_b \left(\frac{4\nu_0 r_{ab} \bullet \nabla_a W_{ab}}{(\rho_a + \rho_b)\left(r_{ab}^2 + 0.01h^2\right)}\right) v_{ab} + \sum_b m_b \left(\frac{\tau_a^{ij} + \tau_b^{ij}}{\rho_a \bullet \rho_b}\right) \nabla^i W_{ab} \tag{17}$$

where, v_o is kinematic viscosity, and τ^{ij} is the SPS stress tensor in Einstein notation. In terms of Einstein notation in coordinate directions i and j, τ is expressed as:

$$\frac{\tau^{ij}}{\rho} = 2\nu_{SPS}\left(s^{ij} - \frac{1}{3}s^{ij}\delta^{ij}\right) - \frac{2}{3}C_{L,SPH}\Delta^2\delta^{ij}\left|s^{ij}\right|^2 \tag{18}$$

The turbulence eddy viscosity is $\nu_{SPS} = [C_{Sm}\Delta]^2\left|s^{ij}\right|^2$, where $C_{Sm} = 0.12$ represents the Smagorinsky's constant. Δ is the particle spacing at the beginning of the simulation, s^{ij} is an element of the SPS strain tensor (Domínguez et al., 2022), and $C_{L,SPH} = 0.0066$.

3.2.4. Discrete phase modelling in SPH-DEM framework

In the SPH-DEM coupled approach, the motion of a solid particle conveyed by a carrier fluid is determined by examining its interaction with the surrounding fluid numerical particles, using Newton's second law. Thus, the governing equation of motion for particle p at position r_p is:

$$m_p\frac{d^2r_p}{dt^2} = f_p + m_p g + \sum_q f_{c,pq} \tag{19}$$

where, m_p represents the mass of conveyed particle p, f_p is the particle-liquid interaction force exerted on solid particle p by the SPH liquid numerical particles, expressed as (Anderson and Jackson, 1967):

$$f_p = V_p(-\nabla P + \nabla\cdot\tau) + f_d(\in_p, u_s) \tag{20}$$

where, V_p is the volume of the solid particle. Fluid forces such as shear stress and buoyancy are represented by the first two terms in Eq. (20). f_d is the particle drag force which is affected by the local porosity $\in_p$ and the superficial velocity u_{Sup}. The u_{Sup} term is defined as:

$$u_{Sup} = \in_p(u_f - u_p) \tag{21}$$

where, u_p is the DEM solid particle velocity and u_f is the fluid velocity. The drag force in the SPH-DEM framework is given by:

$$f_d = \frac{1}{8}C_d \in_p^{-\varphi} \pi d_p^2 \rho_f u_{Sup}\left|u_{Sup}\right| \tag{22}$$

where, ρ_f represents fluid density. C_d is the drag coefficient and φ is a constant, and both are related to the particle Reynolds number, Re_p:

$$C_d = \left(0.63 + \frac{4.8}{\sqrt{Re_p}}\right)^2 \tag{23}$$

$$\varphi = 3.7 - 0.65 \times exp\left[-\frac{\left(1.5 - log_{10}Re_p\right)^2}{2}\right] \tag{24}$$

The third term $f_{c,pq}$ in Eq. (19) represents the collision force between conveyed solid particles p and q, as modelled by the DEM module discussed above. Note, in Eq. (10), $\vec{F}_{DEM,pq}$ is replaced by $\sum_q f_{c,pq}$.

4. Simulation implementation and execution

The numerical parameters used in the CFD-DEM and SPH-DEM simulations are listed in Table 2, where the DEM parameters are the same for both approaches.

4.1. Boundary conditions

When simulating either single-phase or two-phase flow, CFD requires

Table 2
Modelling parameters used in CFD-DEM and SPH-DEM simulations.

Solid phase	CFD-DEM	SPH-DEM
Young's modulus (kPa)	400	400
Passion ratio (-)	0.5	0.5
Restitution coefficient (-)	0.75	0.75
Friction coefficient (-)	0.4	0.4
Numerical particle spacing, s_p (m)	–	0.0006
Overlap distance (m)	$0.02d_p$	$0.5s_p$
Time step, Δt_{DEM} (s)	0.0001	0.000005
Liquid phase		
Papanastasiou parameter, m (-)	–	10
Power-law index, n (-)	0.89	0.89
Mesh size (m)	0.001–0.004	–
Numerical particle spacing (m)	–	0.0006
Kernel function	–	Wendland
Kernel smooth length, h (m)	–	$h = 0.1 \cdot \sqrt{3} s_p$
Time step, Δt_{Liquid} (s)	0.001	0.000005

a uniform liquid velocity field at the pipe inlet and a specified pressure at the outlet, and the no-slip condition is applied to the liquid phase at the pipe wall. In particle-liquid flow, a particle–wall collision model is applied.

In SPH, periodic boundary conditions are applied at the inlet and outlet of the pipe in all single-phase and two-phase simulations, which reduces computational work significantly (Gomez-Gesteira et al., 2012). Buffer layers are implemented to enforce open boundaries at the inlet and outlet, as shown in Fig. 4, which serve to mitigate errors that arise due to kernel truncation near boundaries. Within these buffer regions, particles are introduced or removed to avoid the occurrence of voids. The physical quantities of the buffer numerical particles, such as velocity and pressure, can be extrapolated from the fluid domain. The numerical representation of the wall boundary introduces a set of boundary particles. In SPH cases, forty layers of such particles were utilized.

The dynamic boundary condition (DBC) is a standard condition to model the solid surfaces in SPH simulations. DBC addresses the challenge of how to handle the fluid particles near solid boundaries, where traditional SPH particles might not provide an accurate representation due to the absence of neighbouring particles outside the fluid domain. DBC aims to simulate the behaviour of fluid particles at or near boundaries by incorporating the influence of solid surfaces on the fluid. They ensure that the boundary conditions, such as no-slip or non-penetration conditions are satisfied, even though no physical fluid particles might exist at the exact boundary position. In DBC, a stationary solid is efficiently depicted using fixed particles, wherein their pressure is derived from the equation of state (Eq. (14). The establishment of DBC is simple, facilitating stable and efficient computations that offer a robust numerical framework for simulating intricate geometries. Nevertheless, a small unphysical gap between the fluid and solid boundaries can arise, contributing to a reduction in the precision of pressure measurements along the boundary (English et al., 2022).

Here, a modified dynamic boundary condition (mDBC) was introduced wherein the density of solid particles is acquired through linear extrapolation from ghost positions situated within the fluid domain, as shown in Fig. 4 (English et al., 2022). Through mDBC, the separation between the fluid and boundary is diminished, leading to pressure convergence in undisturbed conditions, including cases involving a sharply cornered bed configuration. The mDBC was used where the boundary interface is located half a particle spacing from the layer of boundary particles closest to the fluid. For each boundary particle, a ghost node was projected into the fluid across the boundary interface.

4.2. Simulation execution

A flowchart depicted in Fig. 5 outlines the execution process of the CFD-DEM and SPH-DEM simulations. In CFD a mesh is first established. Then, the liquid phase is solved by the Navier-Stokes equations. In particle-liquid flow, when the DEM module detects the collision of a particle with another particle or the wall, the CFD-DEM framework estimates the motion of the particle by calculating the forces acting on it and feeds back to the liquid phase. Then, both the particle and liquid phase properties are updated. The simulation ends when the target execution time (t_{target}) is reached.

The SPH simulations follow a similar flowchart as CFD. However, numerical particles are first generated, and the liquid phase is estimated by creating a particle neighbours list. In particle-liquid flow, when the DEM module detects the collision of a particle with another particle or the wall, the SPH-DEM estimates the particle movement and feeds back to the liquid phase. The properties of the solid/liquid phases are then updated. The simulation stops once t_{target} is reached.

A mesh independence study was conducted for CFD and, correspondingly, a numerical particle independence study was conducted for

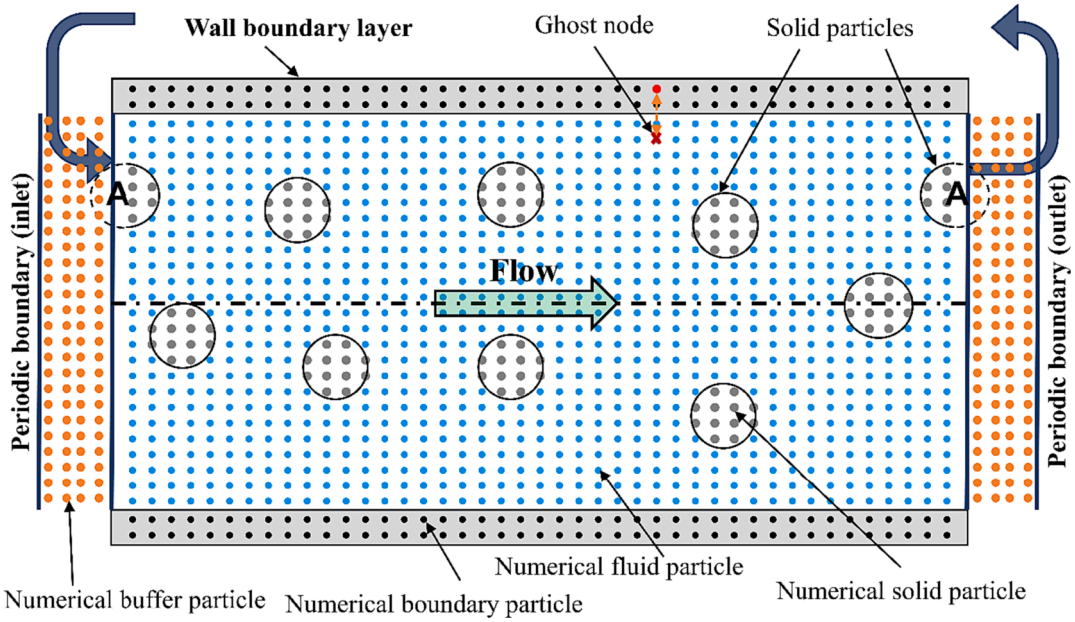

Fig. 4. Schematic of the boundary conditions in the SPH method.

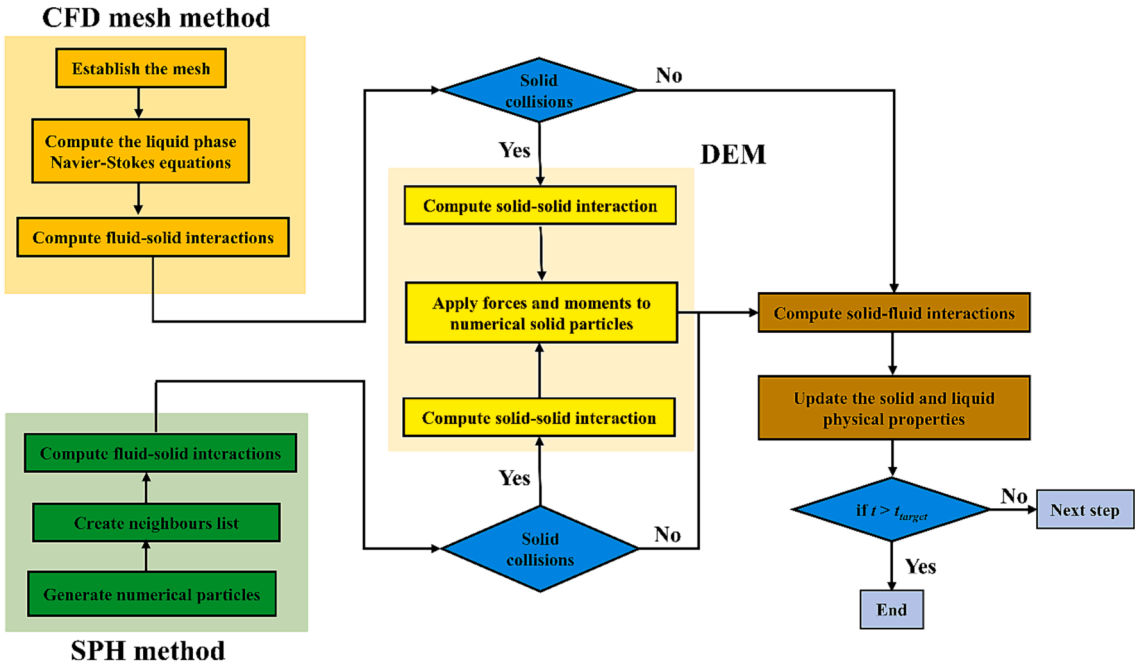

Fig. 5. Flowchart of the CFD-DEM and SPH-DEM approaches.

SPH for a range of Reynolds numbers in single-phase flow. The optimal conditions obtained were: ~ 250,000 mesh cells for CFD and ~ 535000 numerical particles for SPH.

5. Results and discussion

To thoroughly assess the capability and performance of both the mesh-based CFD method and meshfree particle-based SPH method, we investigated single-phase and two-phase particle-liquid flows of various levels of complexity, including: (i) single-phase viscous flow of Newtonian fluids as well as non-Newtonian fluids represented by various rheology models, namely power-law, Bingham plastic and Herschel-Bulkley covering a wide range of rheological parameters; (ii) single-phase turbulent flow of Newtonian fluids; and (iii) particle-laden flows in both the viscous and turbulent regimes, by coupling both the CFD and SPH techniques with a DEM module. Finally, a comprehensive computational cost analysis of these two methods was conducted.

In both single-phase and two-phase flow, the Eulerian liquid phase

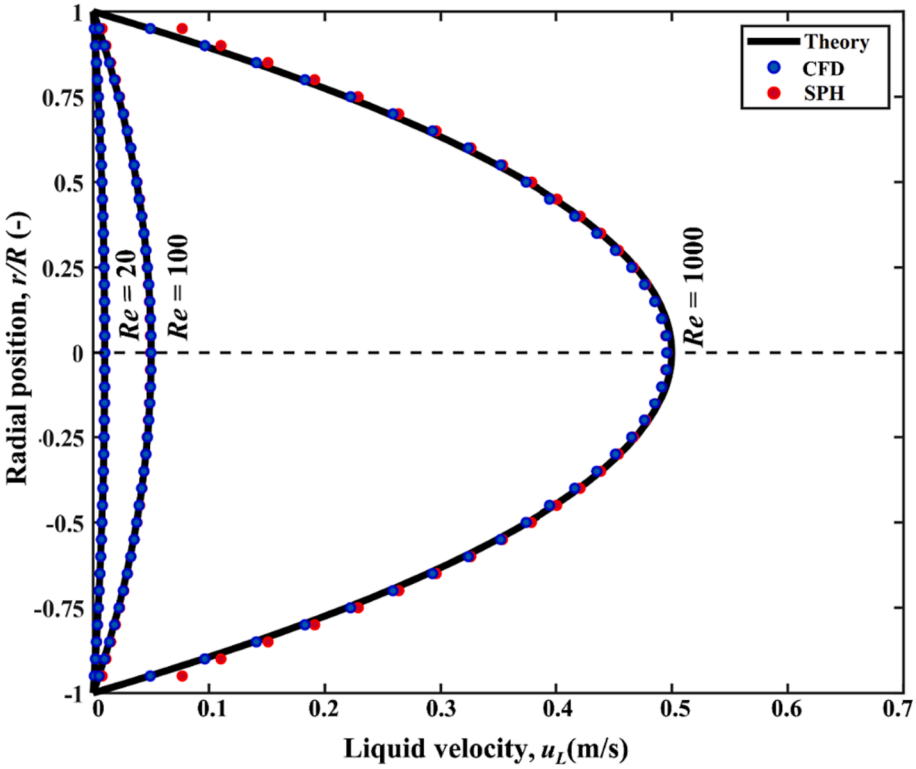

Fig. 6. CFD and SPH predictions of radial velocity profile in laminar Newtonian flow compared to analytical solution: $\rho_L = 1000$ kg m^{-3}; $\mu_L = 0.001$ Pa s.

results obtained from the CFD or CFD-DEM simulations were extracted from the middle cross-section plane of the pipe, while the Lagrangian solid particle data were obtained 3 m downstream of the inlet of the numerical pipe geometry which is an exact replicate of the experimental pipe (Fig. 1). Data processing utilised the radial averaging method mentioned in section 2.3. The SPH or SPH-DEM data were acquired by gathering the physical quantities of all liquid and solid particles within the pipe over a period of 3–5 s, after the simulation had stabilized. The liquid and solid Lagrangian data in SPH-DEM were statistically analysed and post-processed based on the pipe sectioning described in Fig. 2.

5.1. Laminar flow of single-phase fluids of varying rheology

5.1.1. Newtonian fluids

The radial velocity profiles predicted by CFD and SPH at Reynolds numbers (*Re*) from 20 to 1000 are presented in Fig. 6, alongside their corresponding theoretical parabolic profiles (Bird et al., 1977). Overall, the plots show very good agreement between simulation data and theory. However, whilst CFD results demonstrate excellent adherence to the theoretical profiles, SPH results exhibit a minor deviation (overestimation) near the pipe wall which may be attributed to the fact that the SPH wall boundary gives a reasonable approximation of the no-slip condition but does not perfectly enforce it.

5.1.2. Power-law fluids

The radial velocity profiles predicted by CFD and SPH for power-law fluids of varying flow behaviour index (n) are plotted in Fig. 7, alongside their analytical solutions (Bird et al., 1977). Over a wide range of n values from 0.6 to 1.4, CFD produces excellent predictions matching very closely the theoretical velocity profiles across almost the entire pipe cross-section. The SPH method demonstrates very good agreement with the theory in the central region, but displays some significant near the wall, probably arising from the approximated treatment of the no-slip condition, as pointed out above.

5.1.3. Bingham plastic fluids

In the flow of Bingham plastic fluids, a critical parameter is the apparent yield stress (τ_y) which is the variable under investigation here, while the fluid consistency index (k_f) is kept constant. As shown in Fig. 8, both CFD and SPH exhibit excellent agreement with the theoretical predictions over a range of τ_y values from 1 to 7 Pa, particularly in the central plug region. However, there SPH yields tends to underestimate the fluid velocity in the vicinity of the wall compared to the theoretical solution. Despite incorporating more accurate modified dynamic boundary condition, the predictive ability of SPH near the wall still requires further refinement. This limitation is attributed to the current state-of-the art of the meshfree particle-based method, wherein 3D curved surface boundaries need further improvement (English et al., 2022).

5.1.4. Herschel Bulkley fluids

Results for the Herschel Bulkley rheological model are depicted in Fig. 9 for a range of n values from 0.6 to 1.4. Notably, both CFD and SPH exhibit excellent accuracy compared to theory.

5.2. Turbulent flow of single-phase Newtonian fluids

The capability and predictive performance of CFD and SPH is examined in the turbulent regime across a range of Reynolds numbers from 4,500 to 108,000 and presented in Fig. 10. At low turbulence (Re = 4500), slightly above the transition regime, both CFD and SPH exhibit good agreement across most of the pipe cross-section with the well-known theoretical one-seventh power law relationship which is valid for 4500 < Re < 20000 (De Chant, 2005). At Re = 7800, PEPT data are also shown alongside the one-seventh power law relationship. The CFD predictions coincide very well with the theoretical and experimental results, SPH produces some deviations, particularly in the wall region.

At Re = 12000, the CFD accuracy remains unchanged, but the SPH discrepancies become more significant over most of the pipe radius. At high turbulence (Re = 108000) the one-seventh power law expression

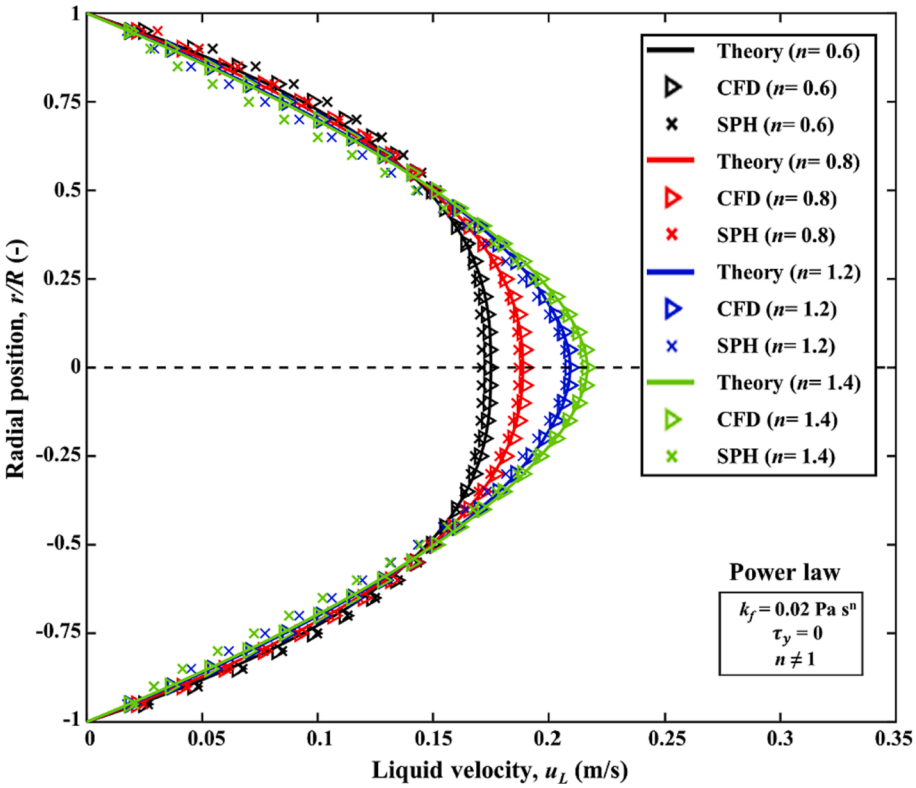

Fig. 7. CFD and SPH predictions of radial velocity profile in laminar flow of different power-law fluids compared to analytical solution.

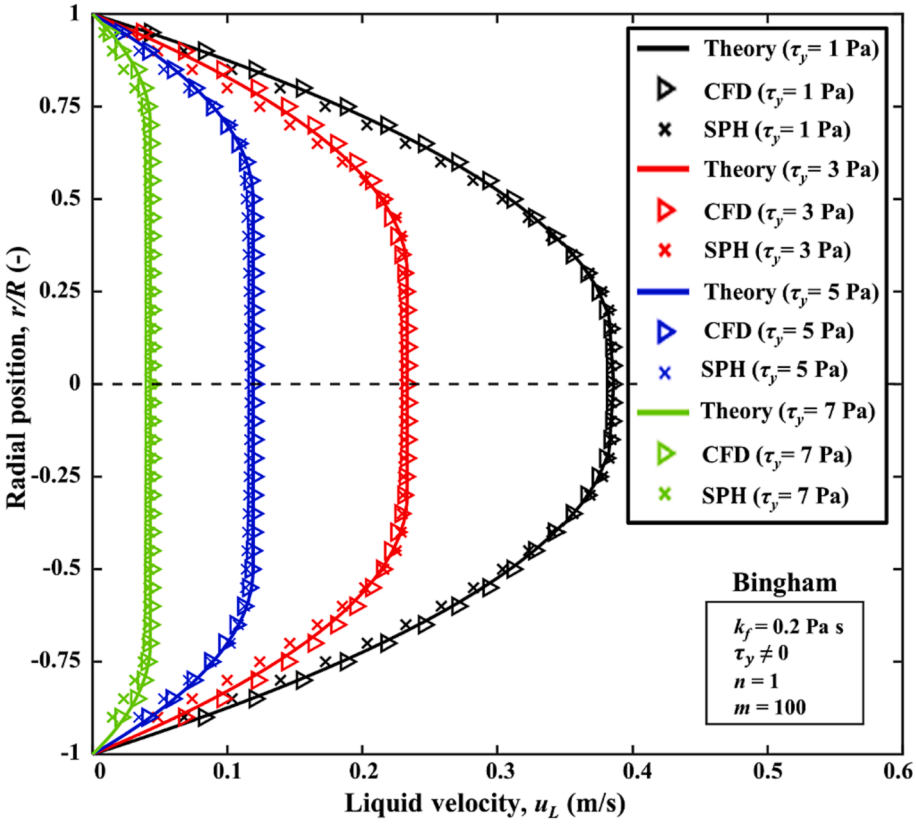

Fig. 8. CFD and SPH predictions of radial velocity profile in laminar flow of different Bingham plastic fluids compared to analytical solution.

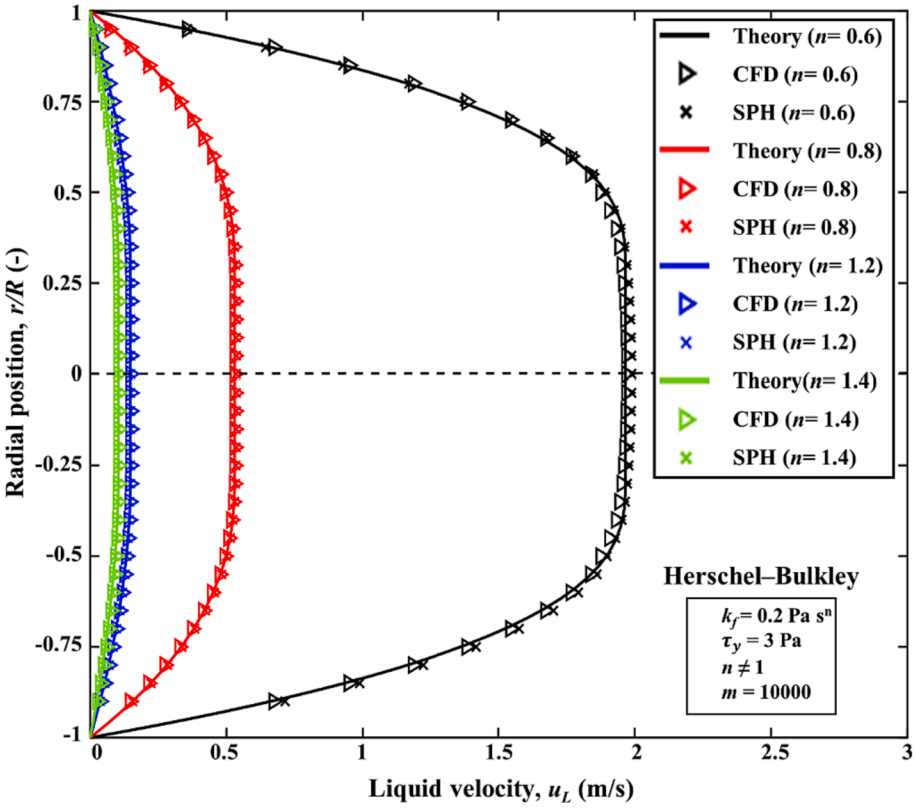

Fig. 9. CFD and SPH predictions of radial velocity profile in laminar flow of different Herschel–Bulkley fluids compared to analytical solution.

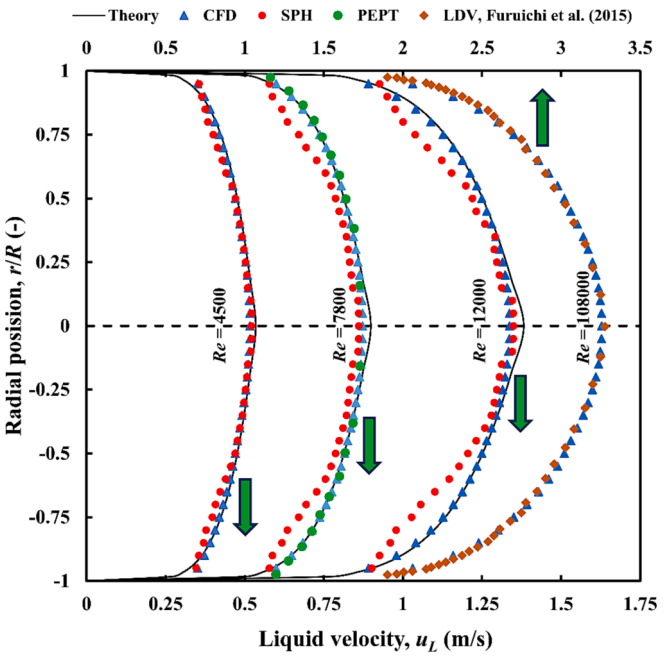

Fig. 10. CFD and SPH predictions of radial velocity profile in turbulent Newtonian flow compared to one-seventh power law correlation and experimental measurements.

does not apply, but the CFD results agree very well with the laser Doppler velocity (LDV) measurements reported by Furuichi et al. (2015). The SPH simulations, on the other hand, failed completely. Although applying the SPS model and shifting algorithm has been reported to improve SPH stability and precision for treating turbulent flows, the method encountered serious challenges in achieving accurate results for $Re > 12000$ (Vacondio et al., 2013). The ability of SPH to simulate turbulent flows is limited at present because of the lack of appropriate turbulence models. This is an area in need of further development.

5.3. Particle-laden flows

Particle-laden flows were investigated in both the laminar and turbulent flow regimes. The Lagrangian results obtained from the CFD-DEM and the SPH-DEM simulations were subjected to the same analysis procedure employed for PEPT measurements (as described in section 2.3). This procedure was used to obtain radial distributions of local solid and liquid velocities as well as of particle volume concentration.

5.3.1. Laminar flow

Results plotted in Fig. 11 are for two particle concentrations 10 and 30 vol%, with mixture Reynolds number, $Re_{mean} \sim 14$, conveyed by a 0.8 wt% CMC solution. Validation of the numerical simulations is conducted through comparison with PEPT measurements. At the lower concentration ($C_s = 10$ vol%), the CFD-DEM approach produces reasonable predictions of the velocity profile but fails to accurately predict the spatial particle distribution. The near axial symmetry observed in the CFD-DEM particle velocity and volume concentration profiles suggest inadequate estimation of particle gravity settling effects. This discrepancy warrants further investigation and improvement. However, at high solid loading ($C_s = 30$ vol%), the CFD-DEM method manages to predict particle velocity and concentration distribution to a good degree of accuracy. In contrast, the SPH-DEM method is more successful in predicting the particle velocity and concentration profiles at both low and high solid loadings, indicating a superior capability over

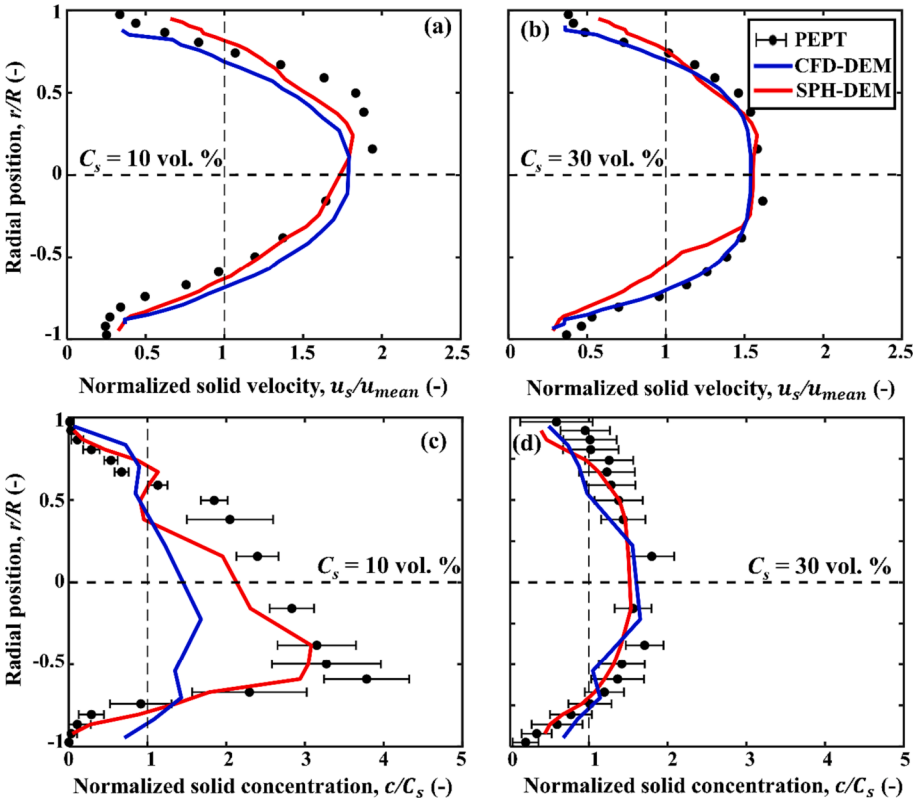

Fig. 11. CFD-DEM and SPH-DEM predictions compared to PEPT measurements in laminar particle-laden flow ($d_p = 4$ mm and $\rho_r = 1.014$, $Re_{mean} = 14$): (a) particle velocity profile ($C_s = 10$ vol%); (b) particle velocity profile ($C_s = 30$ vol%); (c) particle concentration distribution ($C_s = 10$ vol%); (d) particle concentration distribution ($C_s = 30$ vol%). Note velocity error bars are too small to be shown.

CFD-DEM in the laminar regime.

5.3.2. Turbulent flow

The case displayed in Fig. 12 is for 30 vol% solids conveyed by a 36 wt% sugar solution, at a mean mixture Reynolds number of 7800. Bar some slight deviations near the wall, the CFD-DEM method demonstrates a close match with PEPT results over most of the pipe cross-section, accurately estimating particle and liquid velocities, as well as particle concentration. The predictions of particle velocity and concentration distributions by SPH-DEM agree well with PEPT results, albeit with slight discrepancies near the pipe wall. However, the liquid velocity profile exhibits a significant deviation from the PEPT profile away from the central core region. Thus, the CFD-DEM model framework appears to be better at handling particle-laden turbulent flows compared to SPH-DEM. At lower Reynolds numbers, the agreement between CFD-DEM and SPH-DEM improves somewhat, as exemplified in Fig. 13.

5.4. Computational cost

Computational cost serves as a crucial metric for assessing the cost-effectiveness of numerical simulations in practical applications. Recent advancements in computer science have led to significant increases in both CPU and GPU computational power, making the implementation of CPU-GPU solutions possible. An illustrative study utilizing 12 CPUs (Intel® Xeon® Silver 4214 Processor) and a GPU (NVIDIA® GeForce® RTX 2080) was used to estimate the computational time for different numerical CFD-DEM and SPH-DEM simulations, as summarised in Table 3. For single-phase flow ($Re = 100$, section 5.1.1) using the CFD-DEM method, the computational time was negligible. The utilization of GPU further reduced the processing time. However, for particle-laden flow ($C_s = 30$ vol%, section 5.3.1), a much longer computation time (~3 orders of magnitude greater) was necessary, which could be moderately reduced (~16 %) with the aid of GPU.

SPH-DEM proved very inefficient compared to CFD-DEM, requiring ~ 250 times longer without GPU and ~ 13 times longer with GPU for single-phase flow, and ~ 16 times and ~ 6 times more computational time without and with GPU, respectively, for particle-liquid flow.

It is noteworthy that in the case of SPH-DEM, the use of GPU technology produced much greater improvements performance compared to CPU alone, proving highly suitable for meeting the computational demands of large-scale smoothed particle simulations (Winkler et al., 2017; Xiong et al., 2013). Thus, mesh-based CFD demonstrates high cost-effectiveness compared to SPH.

6. Conclusion

In this study, we explored the capabilities and performance of mesh-based CFD and meshfree particle-based SPH coupled with DEM in simulating single-phase and particle-liquid pipe flows. Through a comprehensive analysis encompassing laminar and turbulent flow regimes, various fluid rheologies, and particle-laden scenarios, we shed light on the strengths and limitations of each approach. In single-phase flow, the CFD method demonstrated excellent concordance with theoretical models and provided accurate predictions across various scenarios including laminar and turbulent regimes. Meanwhile, the SPH method, despite approximations in boundary conditions, excelled in capturing complex fluid dynamics, especially in laminar flows. The ability of SPH to simulate turbulent flows is limited at present because of the lack of appropriate turbulence models. This is an area which needs further development.

Coupling both methods with the DEM method enhanced the capabilities of both techniques for simulating particle-laden flows. Validation against PEPT experimental data showcased the reliability of the methods, especially in the laminar regime and at low/moderate turbulence. An illustrative computational cost analysis showed that the CFD method was more cost-effective, while the SPH method can offer more detailed fluid dynamics insights at the expense of longer computational times. This study has served to advance our understanding of these numerical methods and their capability to simulate complex multiphase fluid flows, providing valuable guidance for future research and

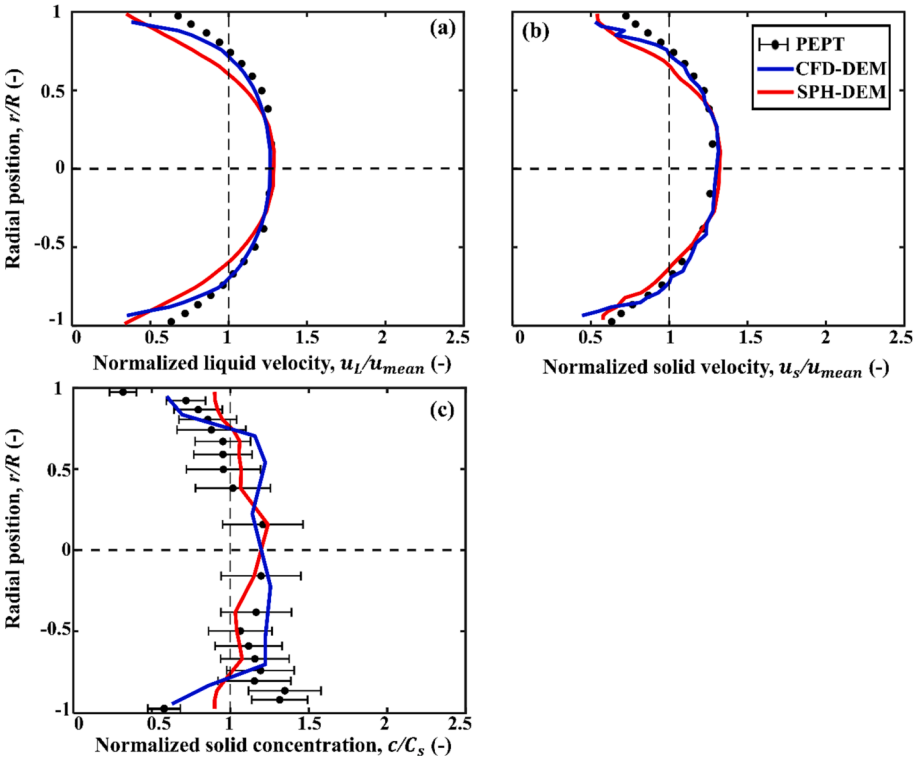

Fig. 12. CFD-DEM and SPH-DEM predictions compared to PEPT measurements in turbulent particle-laden flow ($d_p = 4$ mm, $C_s = 30$ vol%, $\rho_r = 1.02$, $Re = 7800$): (a) liquid velocity profile; (b) particle velocity profile; (c) particle concentration distribution. Note velocity error bars are too small to be shown.

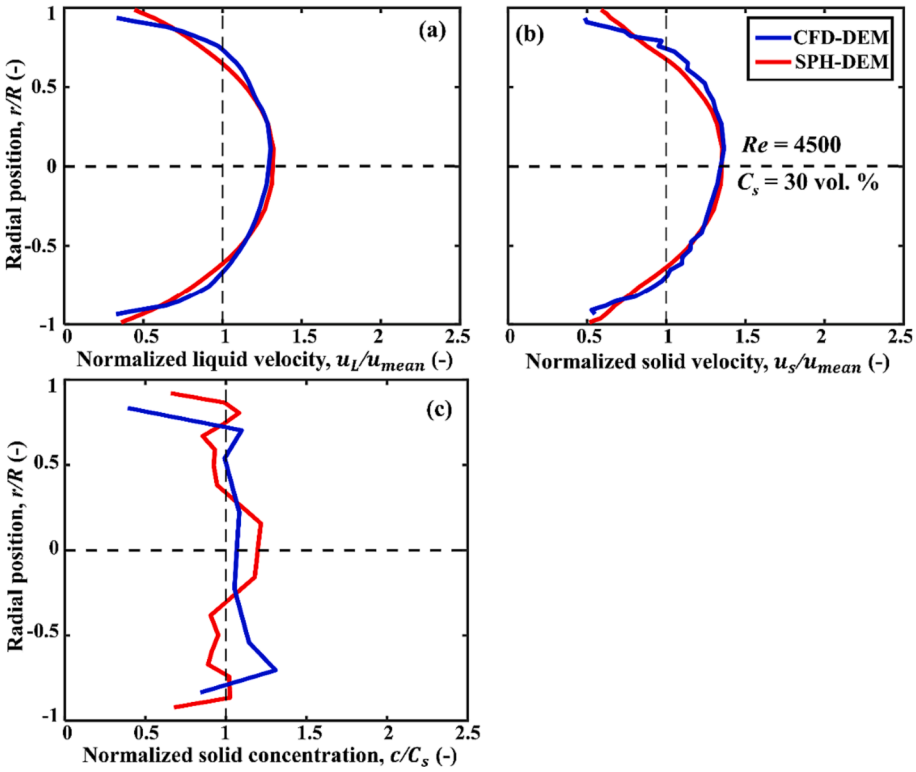

Fig. 13. CFD-DEM and SPH-DEM predictions compared in turbulent particle-laden flow ($d_p = 4$ mm, $C_s = 30$ vol%, $\rho_r = 1.02$, $Re = 4500$): (a) liquid velocity profile; (b) particle velocity profile; (c) particle concentration distribution.

Table 3
Illustrative comparison of computational cost of CFD-DEM and SPH-DEM.

	Single-phase flow			Particle-laden flow		
	Number of mesh/numerical particles	Simulation time (hr)		Number of mesh/numerical particles	Simulation time (hr)	
		CPU	CPU-GPU		CPU	CPU-GPU
CFD-DEM	228456	0.05	0.03	255592	23.6	19.7
SPH-DEM	533019	12.6	0.4	795488	372	127

Mostafa Barigou reports financial support was provided by Engineering and Physical Sciences Research Council.

practical applications.

CRediT authorship contribution statement

ZhuangJian Yang: Conceptualization, Data curation, Formal analysis, Investigation, Software, Validation, Visualization, Writing – original draft. **Xue Lian:** Conceptualization, Data curation, Formal analysis, Investigation, Software, Validation, Visualization, Writing – original draft. **Chiya Savari:** Conceptualization, Formal analysis, Investigation, Methodology, Validation, Visualization, Writing – review & editing. **Mostafa Barigou:** Conceptualization, Formal analysis, Funding acquisition, Methodology, Project administration, Resources, Supervision, Validation, Writing – review & editing.

Declaration of competing interest

The authors declare the following financial interests/personal relationships which may be considered as potential competing interests: Mostafa Barigou reports financial support was provided by Engineering and Physical Sciences Research Council.

Data availability

The authors decline to share data

Acknowledgement

This work was supported by EPSRC Programme Grant EP/R045046/1: Probing Multiscale Complex Multiphase Flows with Positrons for Engineering and Biomedical Applications (PI: Prof. M. Barigou, University of Birmingham). ZhuangJian Yang's PhD and Xue Lian's Ph.D. were funded by the University of Birmingham and China Scholarship Council (CSC).

References

Anderson, T.B., Jackson, R., 1967. Fluid mechanical description of fluidized beds. equations of motion. Ind. Eng. Chem. Fundam. 6 (4), 527–539.
Bakalis, S., Cox, P., Wang-Nolan, W., Parker, D., Fryer, p.f., 2003. Use of Positron-Emission Particle Tracking (PEPT) Technique for Velocity Measurements in Model Food Fluids. J. Food Sci. 68 (9), 2684–2692.
Barigou, M., 2004. Particle tracking in opaque mixing systems: An overview of the capabilities of PET and PEPT. Chem. Eng. Res. Des. 82 (9), 1258–1267.
Belytschko, T., Krongauz, Y., Organ, D., Fleming, M., Krysl, P., 1996. Meshless methods: an overview and recent developments. Comput. Methods Appl. Mech. Eng. 139 (1), 3–47.

Bird, R.R., Armstrong, R.C., Hassager, O., 1977. Dynamics of Polymeric Liquids, Volume 1:. Fluid Mechanics. Wiley.
Bose, S., Banerjee, M., 2015. Effect of non-Newtonian characteristics of blood on magnetic particle capture in occluded blood vessel. J. Magn. Magn. Mater. 374, 611–623.
Cundall, P.A., Strack, O.D., 1979. A discrete numerical model for granular assemblies. Geotechnique 29 (1), 47–65.
Dalrymple, R.A., Rogers, B., 2006. Numerical modeling of water waves with the SPH method. Coast. Eng. 53 (2–3), 141–147.
De Chant, L.J., 2005. The venerable 1/7th power law turbulent velocity profile: a classical nonlinear boundary value problem solution and its relationship to stochastic processes. Appl. Math Comput. 161 (2), 463–474.
Dennis, S., Singh, S., Ingham, D., 1980. The steady flow due to a rotating sphere at low and moderate Reynolds numbers. J. Fluid Mech. 101 (2), 257–279.
Domínguez, J.M., Fourtakas, G., Altomare, C., Canelas, R.B., Tafuni, A., García-Feal, O., Martínez-Estévez, I., Mokos, A., Vacondio, R., Crespo, A.J., 2022. DualSPHysics: from fluid dynamics to multiphysics problems. Computational Particle Mechanics 9 (5), 867–895.
Drew, D.A., 1993. Analytical modeling of multiphase flow. Particulate two-phase flow.
Duan, G., Chen, B., Koshizuka, S., Xiang, H., 2017. Stable multiphase moving particle semi-implicit method for incompressible interfacial flow. Comput. Methods Appl. Mech. Eng. 318, 636–666.
Eesa, M., Barigou, M., 2008. Horizontal laminar flow of coarse nearly-neutrally buoyant particles in non-Newtonian conveying fluids: CFD and PEPT experiments compared. Int. J. Multiph. Flow 34 (11), 997–1007.
El-Emam, M.A., Zhou, L., Shi, W., Han, C., Bai, L., Agarwal, R., 2021. Theories and applications of CFD–DEM coupling approach for granular flow: a review. Arch. Comput. Meth. Eng. 28 (7), 4979–5020.
English, A., Domínguez, J., Vacondio, R., Crespo, A., Stansby, P., Lind, S., Chiapponi, L., Gómez-Gesteira, M., 2022. Modified dynamic boundary conditions (mDBC) for general-purpose smoothed particle hydrodynamics (SPH): application to tank sloshing, dam break and fish pass problems. Computational Particle Mechanics 9 (5), 1–15.
Fairhurst, P.G., Barigou, M., Fryer, P.J., Pain, J.P., Parker, D.J., 2001. Using positron emission particle tracking (PEPT) to study nearly neutrally buoyant particles in high solid fraction pipe flow. Int. J. Multiph. Flow 27 (11), 1881–1901.
Fluent, A., 2011. Ansys fluent theory guide. Ansys Inc. USA 15317, 431–432.
Fourtakas, G., Dominguez, J.M., Vacondio, R., Rogers, B.D., 2019. Local uniform stencil (LUST) boundary condition for arbitrary 3-D boundaries in parallel smoothed particle hydrodynamics (SPH) models. Comput. Fluids 190, 346–361.
Furuichi, N., Terao, Y., Wada, Y., Tsuji, Y., 2015. Friction factor and mean velocity profile for pipe flow at high Reynolds numbers. Phys. Fluids 27 (9), 095108.
Gomez-Gesteira, M., Rogers, B.D., Dalrymple, R.A., Crespo, A.J., 2010. State-of-the-art of classical SPH for free-surface flows. J. Hydraul. Res. 48 (sup1), 6–27.
Gomez-Gesteira, M., Rogers, B.D., Crespo, A.J., Dalrymple, R.A., Narayanaswamy, M., Dominguez, J.M., 2012. SPHysics–development of a free-surface fluid solver–Part 1: theory and formulations. Comput. Geosci. 48, 289–299.
Gosman, A., Loannides, E., 1983. Aspects of computer simulation of liquid-fueled combustors. Journal of Energy 7 (6), 482–490.
Guida, A., Nienow, A.W., Barigou, M., 2010. PEPT measurements of solid–liquid flow field and spatial phase distribution in concentrated monodisperse stirred suspensions. Chem. Eng. Sci. 65 (6), 1905–1914.
Guida, A., Nienow, A.W., Barigou, M., 2011. Mixing of dense binary suspensions: multi-component hydrodynamics and spatial phase distribution by PEPT. AIChE J 57 (9), 2302–2315.
Han, Z., Su, B., Li, Y., Dou, J., Wang, W., Zhao, L., 2020. Modeling the progressive entrainment of bed sediment by viscous debris flows using the three-dimensional SC-HBP-SPH method. Water Res. 182, 116031.
Hertz, H., 1882. Ueber die Berührung fester elastischer Körper.
Kong, D., Zhou, M., Wang, S., Luo, K., Li, D., Fan, J., 2021. Eulerian-Lagrangian simulation of chemical looping combustion with wide particle size distributions. Chem. Eng. Sci. 245, 116849.
Koshizuka, S., Oka, Y., 1996. Moving-particle semi-implicit method for fragmentation of incompressible fluid. Nucl. Sci. Eng. 123 (3), 421–434.
Li, K., Savari, C., Barigou, M., 2022. Computation of Lagrangian coherent structures from experimental fluid trajectory measurements in a mechanically agitated vessel. Chem. Eng. Sci. 254, 117598.
Li, K., Savari, C., Barigou, M., 2023a. Predicting complex multicomponent particle–liquid flow in a mechanically agitated vessel via machine learning. Phys. Fluids 35 (5).
Li, K., Savari, C., Sheikh, H.A., Barigou, M., 2023b. A data-driven machine learning framework for modeling of turbulent mixing flows. Phys. Fluids 35 (1).
Lian, X., Savari, C., Li, K., Barigou, M., 2023. Coupled smoothed particle hydrodynamics and discrete element method for simulating coarse food particles in a non-Newtonian conveying fluid. Phys. Fluids 35 (4).
Liu, L., Barigou, M., 2013. Numerical modelling of velocity field and phase distribution in dense monodisperse solid–liquid suspensions under different regimes of agitation: CFD and PEPT experiments. Chem. Eng. Sci. 101, 837–850.
Liu, M., Liu, G., 2010. Smoothed particle hydrodynamics (SPH): an overview and recent developments. Arch. Comput. Meth. Eng. 17, 25–76.
Liu, K.-S., Sheu, T.-W.-H., Hwang, Y.-H., Ng, K.-C., 2017. High-order particle method for solving incompressible Navier-Stokes equations within a mixed Lagrangian-Eulerian framework. Comput. Methods Appl. Mech. Eng. 325, 77–101.
Lo, E.Y., Shao, S., 2002. Simulation of near-shore solitary wave mechanics by an incompressible SPH method. Appl. Ocean Res. 24 (5), 275–286.
Lucy, L.B., 1977. A numerical approach to the testing of the fission hypothesis. Astronomical Journal, vol. 82, Dec. 1977, p. 1013-1024. 82, 1013-1024.
Menter, F.R., Kuntz, M., Langtry, R., 2003. Ten years of industrial experience with the SST turbulence model. Turbulence, Heat and Mass Transfer 4 (1), 625–632.
Messa, G.V., Matoušek, V., 2020. Analysis and discussion of two fluid modelling of pipe flow of fully suspended slurry. Powder Technol. 360, 747–768.
Mindlin, R.D., 1949. Compliance of elastic bodies in contact.
Monaghan, J.J., 2005. Smoothed particle hydrodynamics. Rep. Prog. Phys. 68 (8), 1703.
Nguyen, N.H., Nguyen, T.T., Phan, Q.T., 2022. Dynamics and runout distance of saturated particle-fluid mixture flow on a horizontal plane: a coupled VOF-DEM study. Powder Technol. 408, 117759.
Pianko-Oprych, P., Nienow, A., Barigou, M., 2009. Positron emission particle tracking (PEPT) compared to particle image velocimetry (PIV) for studying the flow generated by a pitched-blade turbine in single phase and multi-phase systems. Chem. Eng. Sci. 64 (23), 4955–4968.
Robinson, M.J., 2009. Turbulence and viscous mixing using smoothed particle hydrodynamics. Monash University.
Savari, C., Barigou, M., 2022. Lagrangian wavelet analysis of turbulence modulation in particle–liquid mixing flows. Phys. Fluids 34 (11).
Savari, C., Sheikh, H.A., Barigou, M., 2021. Lagrangian recurrence tracking: a novel approach for description of mixing in liquid and particle–liquid flows. Ind. Eng. Chem. Res. 60 (50), 18501–18512.
Savari, C., Li, K., Barigou, M., 2022. Multiscale wavelet analysis of 3D Lagrangian trajectories in a mechanically agitated vessel. Chem. Eng. Sci. 260, 117844.
Sharaf, O.Z., Al-Khateeb, A.N., Kyritsis, D.C., Abu-Nada, E., 2019. Numerical investigation of nanofluid particle migration and convective heat transfer in microchannels using an Eulerian-Lagrangian approach. J. Fluid Mech. 878, 62–97.
Sheikh, H.A., Savari, C., Barigou, M., 2022a. A data-driven stochastic model for velocity field and phase distribution in stirred particle-liquid suspensions. Powder Technol. 411, 117940.
Sheikh, H.A., Savari, C., Barigou, M., 2022b. Lagrangian stochastic modelling of liquid flow in a mechanically agitated vessel. Chem. Eng. Sci. 249, 117318.
Tian, S., Barigou, M., 2016. Assessing the potential of using chaotic advection flow for thermal food processing in heating tubes. J. Food Eng. 177, 9–20.
Tsuji, Y., Oshima, T., Morikawa, Y., 1985. Numerical simulation of pneumatic conveying in a horizontal pipe. Kona Powder Part. J. 3, 38–51.
Vacondio, R., Rogers, B.D., Stansby, P.K., Mignosa, P., Feldman, J., 2013. Variable resolution for SPH: a dynamic particle coalescing and splitting scheme. Comput. Methods Appl. Mech. Eng. 256, 132–148.
Winkler, D., Meister, M., Rezavand, M., Rauch, W., 2017. gpuSPHASE—A shared memory caching implementation for 2D SPH using CUDA. Comput. Phys. Commun. 213, 165–180.
Xiong, Q., Li, B., Xu, J., 2013. GPU-accelerated adaptive particle splitting and merging in SPH. Comput. Phys. Commun. 184 (7), 1701–1707.
Yang, Z., Savari, C., Barigou, M., 2022. Numerical and Experimental Investigations of Horizontal Turbulent Particle–Liquid Pipe Flow. Industrial & engineering chemistry research.
Ye, T., Pan, D., Huang, C., Liu, M., 2019. Smoothed particle hydrodynamics (SPH) for complex fluid flows: recent developments in methodology and applications. Phys. Fluids 31 (1).
Yeoh, G.H., Tu, J., 2019. Computational techniques for multiphase flows. Butterworth-Heinemann.
Zbib, H., Ebrahimi, M., Ein-Mozaffari, F., Lohi, A., 2018. Comprehensive analysis of fluid-particle and particle-particle interactions in a liquid-solid fluidized bed via CFD-DEM coupling and tomography. Powder Technol. 340, 116–130.
Zheng, E., Rudman, M., Kuang, S., Chryss, A., 2021. Turbulent coarse-particle non-Newtonian suspension flow in a pipe. Int. J. Multiph. Flow 142, 103698.